Plasma Physics and
Controlled Fusion

PURPOSE-LED
PUBLISHING™

**PAPER** • **OPEN ACCESS**

# Plasma rotation and thermonuclear neutron emission estimates in JET deuterium tritium plasmas from neutron spectroscopy

To cite this article: Linus Hägg *et al* 2025 *Plasma Phys. Control. Fusion* **67** 035024

View the article online for updates and enhancements.

You may also like

- First observations of edge instabilities in strongly shaped negative triangularity plasmas on DIII-D
T Cote, G Yu, A O Nelson et al.
- Drastic effects of $N_2$ addition in the chemical composition of $C_2H_2$/Ar glow discharges
Isabel Tanarro, Ramón J Peláez and Víctor J Herrero
- Resilient stellarator divertor characteristics in the Helically Symmetric eXperiment
K A Garcia, A Bader, D Boeyaert et al.

This content was downloaded from IP address 130.238.188.139 on 13/03/2025 at 13:37

OPEN ACCESS
IOP Publishing
Plasma Physics and Controlled Fusion
Plasma Phys. Control. Fusion **67** (2025) 035024 (16pp)
https://doi.org/10.1088/1361-6587/adb5b8

# Plasma rotation and thermonuclear neutron emission estimates in JET deuterium tritium plasmas from neutron spectroscopy

**Linus Hägg[1,*], Jacob Eriksson[1], Sean Conroy[1], Göran Ericsson[1], Krassimir Kirov[2], Erik Andersson Sundén[1] and JET contributors[3]**

[1] Department of Physics and Astronomy, Uppsala University, SE-751 05 Uppsala, Sweden
[2] UKAEA, Culham Science Centre, Abingdon OX143DB, United Kingdom

E-mail: linus.hagg@physics.uu.se

Received 13 December 2024, revised 28 January 2025
Accepted for publication 13 February 2025
Published 25 February 2025

**Abstract**

Data from the magnetic proton recoil spectrometer (MPRu) high-resolution neutron spectrometer has been used to estimate two fusion plasma quantities, the plasma rotation and the thermonuclear neutron emission. This paper presents a framework for this method and the current results for a selection of plasma discharges from the JET DTE3 campaign. Data collection during DTE3 was preceded by a hardware upgrade in the form of new digitizers, and an update to the data reduction software. The method involves simulations with the TRANSP code, the DRESS code, and a detector response function. The plasma rotation and thermonuclear neutron emission are estimated through a fit of the simulated detector response to the MPRu measurement data. This exploratory analysis studied a selection of DTE3 discharges with high neutron rates. It was found that the rotation was typically in the range $1.5 \times 10^5$ to $2.5 \times 10^5$ rad $s^{-1}$ and that neutrons from thermonuclear reactions constitute about 10%–30% of the total neutron emission. For the studied discharges, the neutron emissivity is strongly weighted to the plasma core. Due to the MPRu line of sight passing through the plasma core twice, the plasma rotation and the thermonuclear neutron emission are estimated in the core. This method has the potential to provide complementary data points to other diagnostics.

Keywords: neutron, spectrometer, MPRu, fusion, plasma rotation, JET, thermonuclear emission

[3] See Mailloux *et al* (https://doi.org/10.1088/1741-4326/ac47b4) for JET Contributors.
[*] Author to whom any correspondence should be addressed.

Original content from this work may be used under the terms of the Creative Commons Attribution 4.0 licence. Any further distribution of this work must maintain attribution to the author(s) and the title of the work, journal citation and DOI.


© 2025 The Author(s). Published by IOP Publishing Ltd

## 1. Introduction

Neutron measurements are a key diagnostic in fusion plasma experiments. The deuterium–tritium (DT) fusion reaction produces a neutron with an average energy of 14 MeV. Measurements of the neutron energy spectrum can provide information about the fuel ions in the plasma. High energy-resolution neutron diagnostics can be used to investigate phenomena such as alpha knock-on [1, 2], plasma heating [3, 4], plasma rotation [5], and NBI (Neutral Beam Injection) and Ion Cyclotron Resonance Frequency distribution functions [6, 7]. The magnetic proton recoil spectrometer (MPRu) is such a high-resolution diagnostic and has been in operation at JET since 1996. The MPRu has seen several upgrades over the years, as documented in [8]. This work analyses some of the MPRu data collected during the most recent experimental DT campaign at JET, DTE3 [9]. Models of the neutron energy spectra, together with the spectrometer response function, are used to interpret MPRu measurement data to estimate the plasma rotation and the thermal fraction in the core. The plasma rotation here refers to the toroidal velocity of the thermal bulk plasma, primarily induced by the momentum injected by NBI heating. The plasma rotation estimate is compared to measurement data from the charge exchange (CX) diagnostics at JET [10]. The thermal fraction is defined as the ratio between the neutron emission from thermonuclear reactions[4] and the total neutron emission. This definition relies on the model separating the neutron spectrum into two components, describing the contribution from thermal and supra-thermal ions. The implications of this modelling choice is discussed further in section 5.

Measurements of parameters such as the plasma rotation and the thermal fraction contribute to the theoretical understanding of fusion plasmas. These parameters can be used to validate interpretative plasma modelling codes such as TRANSP. They can also be used directly in analysis of fusion plasma scenarios. ITER scenarios are expected to be dominated by thermal emission, and the thermal fraction can be used to evaluate scenarios that aim to be ITER-relevant in that aspect. Estimates of the plasma rotation have a similar relevance since ITER plasmas are expected to have a generally lower plasma rotation compared to JET [11]. In section 2 we give an overview of the MPRu design, data acquisition system, and data reduction. Section 3 describes the models and simulations used. Section 4 shows our estimates of the plasma rotation and the thermal fraction for a selection of plasma discharges. In section 5 we discuss the potency of the MPRu instrument, limitations of the current work, and potential future prospects.

[4] Thermonuclear reactions are here defined as reactions between two ions from the thermal bulk plasma (as opposed to reactions involving supra-thermal ions from the neutral beam heating and/or radio-frequency heating systems).

## 2. Instrument and measurements

### 2.1. Instrument design

The MPRu instrument is described in detail in [8], but a short summary of its design and components is provided in this section. The MPRu is a thin-foil MPRu with a line of sight (LOS) that passes through the plasma centre twice, with a 47 degree angle to the toroidal magnetic field, see figure 9 in [8]. Neutrons from the fusion plasma arrive through the neutron collimator, see figure 1 in [8], and interact with protons in a hydrogen-rich foil through elastic scattering. Forward-scattered protons—whose energies will to a good approximation be equal to the energies of the corresponding incident neutrons—pass through the proton collimator and into a magnetic system that momentum-separates the protons and focuses them onto an array of scintillators, also known as the hodoscope. The proton's impact point on the array is closely related to its energy.

The detector uses phoswich scintillators [12] which have two scintillating layers with characteristic light-pulse decay times of 1.8 ns and 180 ns. Low-energy protons up to about 5 MeV are stopped in a first, thin scintillator layer, while protons up to 18 MeV penetrate the thin layer and are stopped in the second, thicker scintillator layer. Thus, depending on the range of the protons they will give rise to different, specific scintillation light pulse shapes. This feature is used to improve background rejection. The hodoscope consists of 32 scintillators, see figure 4 in [8], hereafter referred to as hodoscope channels. Channels 1–9 and 23–32 are 20 mm wide and channels 10–22 are 10 mm wide. For the DTE3 campaign, the magnetic field was set such that the 14 MeV peak was centred on the thinner channels.

### 2.2. Data acquisition

Each scintillator is connected to two photomultiplier tubes (PMTs) through lightguides. The two PMT signals are fed to a pulse-summing-amplifier [13] and then into a digitizer, see figure 6 in [8] for the full signal chain. A set of ADQ14 digitizers [14] were installed for the DTE3 campaign, these replaced the transient recorder cards described in [8]. This upgrade increased the digitizer resolution from 8-bits to 14-bits and the sampling frequency from 200 MHz to 1 GHz. The digitizers store the time stamp and full pulse shape for each event, both of which are saved for post-processing in the data reduction procedure.

### 2.3. Data reduction

The MPRu data reduction procedure has been updated since [8] and now consists of a baseline subtraction and a pulse shape discrimination (PSD). An example of the full pulse shape of a recorded event is shown in figure 1.

Each recorded event has 400 samples. The baseline is averaged using samples 10–30 and is subtracted from the whole

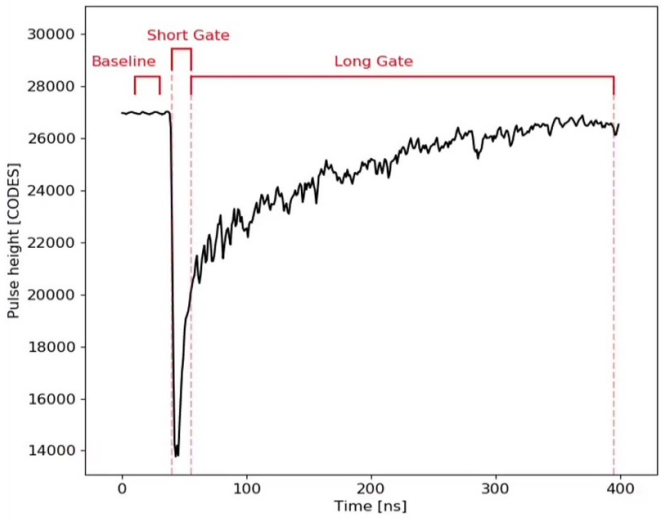


**Figure 1.** Pulse shape for a presumed proton event from JET plasma discharge 104 690, channel 12.

pulse shape. The PSD uses two intervals ('gates') which are showcased in figure 1. The short gate uses samples 40–54 and the long gate uses samples 55–380. Light pulses from the first ('fast') scintillating layer will primarily give a signal in the short gate. Light pulses from the second ('slow') scintillating layer will give a signal in both the short and the long gate. The integrated pulse areas within the short and long gate are referred to as $Q_{\text{short}}$ and $Q_{\text{long}}$ respectively.

The PSD utilizes a 2D histogram with $Q_{\text{short}}$ and $Q_{\text{long}}$ on the axes, where the proton events are separated from the background events. The histogram also reveals features such as pile-up events, escape events, and shadow events. An example 2D PSD histogram and its features are shown in figure 2.

Pile-up events originate from multiple events being detected within the same data record. When their voltage pulses partially or fully overlap within a data record, the resulting $Q_{\text{long}}$ value is larger for pile-up events.

Escape events and shadow events are cases where a proton deposits energy in two adjacent scintillators in the array. An escape event deposits a smaller amount of energy in the second scintillator layer, then leaves the scintillator prematurely and deposits a small amount of its energy in a neighbouring scintillator. This leads to smaller $Q_{\text{long}}$ values compared to a full energy deposition.

Shadow events arrive from an adjacent scintillator and deposits a smaller amount of energy in the first scintillator layer, leading to smaller $Q_{\text{short}}$ values. To avoid double counting, one should not include both escape and shadow events when counting proton events across the hodoscope.

We define the total number of proton events as the events in the proton peak, the pile-up events, and the escape events. The counting process is complicated by the fact that the escape events merge into the background events. In an internal study, Monte Carlo simulations were used to estimate the amount of escape events relative to the total number of proton events [15]. With some variation between the scintillators, the escape events contribute 5%–10% of the total number of proton events. Rather than counting the escape events, one can apply a correction factor based on this ratio. However, this correction is not yet fully implemented. Thus, this work only counts proton events in the proton peak and pile-up events, these are marked in the counting region exemplified in figure 2. All events outside the counting region are considered to be background events, aside from the marked escape events and shadow events. The triangular structure of the background events, as seen in figure 2, is present even when the magnet is switched off, meaning that recoil protons do not reach the hodoscope. However, a characterization of these background features is outside the scope of this paper.

For some channels counting proton events in this manner is fairly straightforward, while for others the proton peak is very close to the background events despite the PSD, see appendix A. By counting proton events in each hodoscope channel, we create a hodoscope histogram, as exemplified in figure 3. The events are expressed in counts/cm, as the proton counts in each channel are divided by the width of their respective detector to better illustrate how events are distributed across the hodoscope. The broadened 14 MeV proton peak is centred between channels 12 and 13.

However, the MPRu hodoscope histogram in figure 3 also reveals a large low-energy component that does not originate from the plasma. The component instead seems to come from neutrons interacting with a layer of paint in the LOS. This paint was applied on various places on the MPRu instrument (including the plasma-facing side of the stainless-steel vacuum window, which is where the fusion neutrons enter the instrument) in 2010. The paint is doped with gadolinium, and was an intervention aimed to reduce background signals from neutron-induced gamma-rays in the hodoscope. However, the paint seems to have had the unintended side effect of constituting an additional source of protons that are produced when the fusion neutrons scatter in the paint on the vacuum window. The protons thus produced then lose some of their energy when passing through the vacuum window, after which they pass through the thin plastic foil and the MPRu magnetic system and are detected on the hodoscope together with the 'ordinary' protons produced in the target foil. Preliminary transport calculations confirm this hypothesis and indicate that this low-energy background component descends quickly above 13 MeV, and should therefore only intrude on the lowest part of the broadened 14 MeV peak. A more detailed report on the origin and modelling of this low-energy MPRu component will be the topic of a future publication.

To avoid the low-energy background component we exclude channel 9 and below in this work, which equates to a threshold at 18 cm in figure 3; the excluded channels are also marked in grey. The error bars in figure 3 are deduced from Poisson statistics, meaning no systematic uncertainties are included.

### 2.4. JET discharges

A few general plasma parameters for the JET discharges covered in this paper are found in table 1. The listed values are averages or ranges representative of the bulk of the discharge.

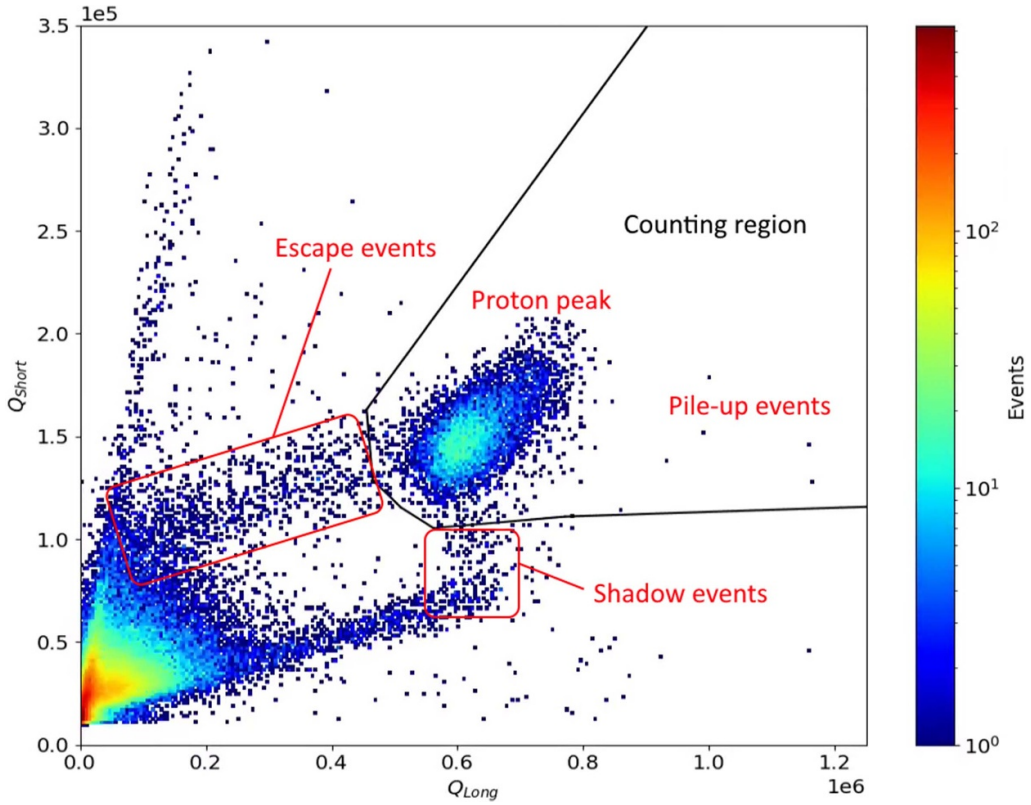


**Figure 2.** 2D PSD histogram for JET plasma discharge 104 681, channel 12, in the time interval 7.0–15.0 s. The proton events from the proton peak and pile-up events are counted by summing all events in the counting region, marked in black.

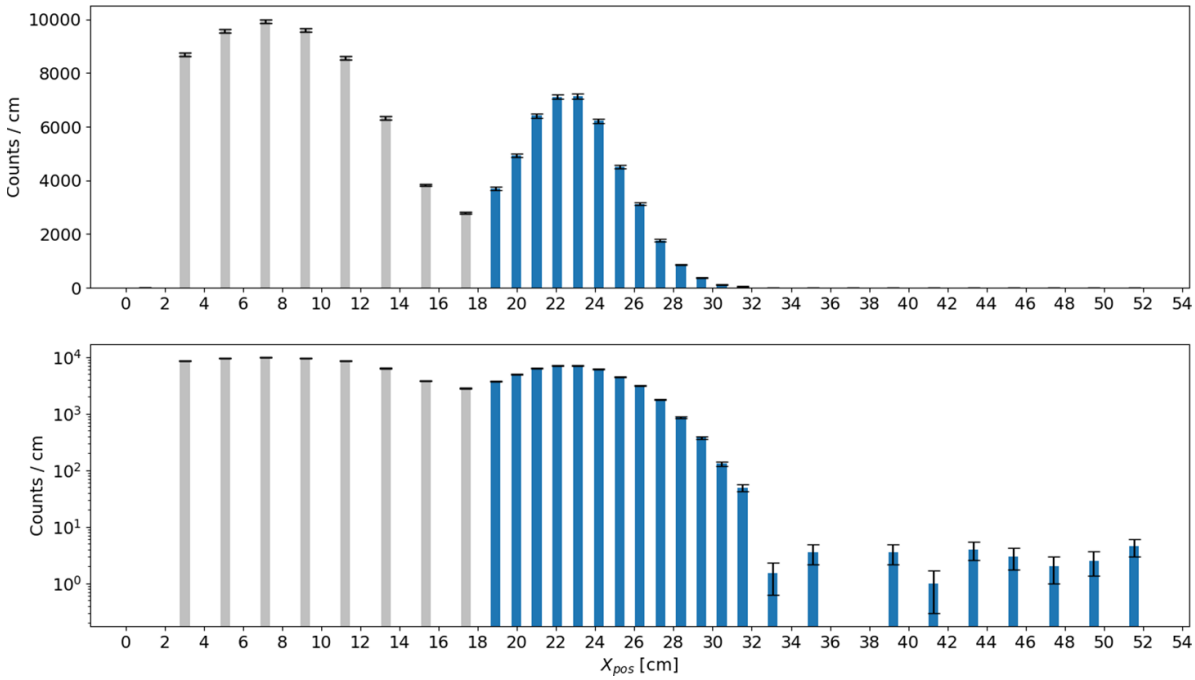


**Figure 3.** Proton peak counts/cm over hodoscope channel positions for JET plasma discharge 104 681 in the time interval 7.0–15.0 s, shown in linear (a) and log scale (b). All hodoscope channels below the 18 cm mark are excluded in this work, in order to avoid the low-energy background component (more details in the main text). The few events above the 32 cm mark are expected to be background and pile-up events in the counting region.

**Table 1.** Overview of general plasma parameters for the reviewed JET plasma discharges.

| JET Plasma discharge # | B-field (T) | Plasma current (MA) | Electron temperature (keV) | Tritium concentration (%) | NBI power (MW) | RF power (MW) |
|---|---|---|---|---|---|---|
| 104 522 | 3.86 | 2.5 | 10.0 | 80 | 29.7 | 5.3 |
| 104 551 | 3.45 | 2.4 | 8.9 | 53 | 27.0 | 3.5 |
| 104 574 | 3.45 | 2.4 | 10.4 | 48 | 27.1 | 4.3 |
| 104 575 | 3.45 | 2.4 | 9.6 | 49 | 27.2 | 4.4 |
| 104 664 | 3.40 | 2.1 | 5.0 | 21–79 | 27.3 | 3.3 |
| 104 674 | 3.85 | 2.7 | 8.5 | 82 | 28.0 | 3.8 |
| 104 675 | 3.85 | 2.5 | 9.0 | 82 | 29.0 | 5.5 |
| 104 676 | 3.40 | 2.1 | 9.0 | 35–92 | 28.0 | 4.0 |
| 104 681 | 3.85 | 2.1 | 7.0–11.0 | 54–63 | 30.0–32.0 | 2.8 |
| 104 689 | 3.43 | 2.3 | 3.5–9.0 | 57–64 | 25.8 | 2.3 |
| 104 690 | 3.43 | 2.3 | 4.0–10.1 | 53–67 | 29.7 | 2.9 |

All discharges used D NBI (Deuterium NBI) and RF (radio-frequency) auxiliary heating, though some measurement data may cover time intervals before these were switched on or after they were switched off, as exemplified in figure 8 in section 4. The tritium concentration values in table 1 were inferred from Penning trap measurements of exhaust gas collected in the divertor [16].

The analysed JET discharges represent a variety of plasma scenarios that were explored during DTE3. Discharges 104 522, 104 664, 104 674, 104 675, 104 676, 104 681, 104 689 and 104 690 were all carried out using the hybrid plasma scenario [17] or its variant with optimized non-thermal fusion [18]. Discharges 104 551, 104 552, 104 574 and 104 575 were part of an experiment characterizing 2nd harmonic RF heating schemes for ITER [19], while 104 668 was part of an experiment aimed at studying energetic alpha particles during the afterglow phase, i.e. immediately after the auxiliary heating has been switched off [20]. (Note that the above references report on results prior to DTE3; they provide the background and aims of the respective experiments, as well as results from the JET DTE2 campaign, but more detailed reports on the DTE3 discharges studied in this paper are not available at the time of writing this paper).

## 3. Modelling and analysis

### 3.1. Neutron spectrum modelling

In order to separate the measured neutron spectrum into the contributions from thermonuclear and supra-thermal emission, we need models of the shapes of the corresponding spectral components[5]. To this end, it is necessary to model the velocity distributions of the D and T fuel ions. For the JET discharges considered in this paper, the relevant distributions will be (i) a Maxwellian distribution for the thermal bulk deuterons, (ii) a Maxwellian distribution for the thermal bulk tritons, and (iii) a supra-thermal distribution of deuterons, arising from the use of D NBI and RF heating tuned to accelerate D ions. Once the distributions are known, the required spectral shapes can be calculated with the DRESS code [21], in which Monte Carlo methods are used to sample the fuel ion distributions and evaluate the resulting neutron energy spectra in the MPRu LOS.

We use the term thermal–thermal component for the neutron spectral component that originates from fusion reactions between two thermal bulk ions. Similarly, we use the term beam–thermal component for that which originates from fusion reactions between a thermal bulk ion and a supra-thermal ion. Fusion reactions between two supra-thermal ions also give rise to a neutron spectral component, which would be the beam–beam component. However, a reaction between two NBI deuterons would produce neutrons with an average energy of 2.5 MeV. With the current magnetic settings, the corresponding recoil protons would not be seen by the hodoscope. Since these events will not be present in the MPRu data, the beam–beam component does not need to be considered in the model.

In this work, we have used the TRANSP code [22–24] to obtain a consistent set of fuel ion distributions. TRANSP takes plasma equilibrium, density and temperature profiles, D/T density fractions, and applied NBI and RF power as input, and uses this data to interpretatively determine the transport of particles, energy and momentum in the plasma. In this process, the slowing-down distribution of the NBI ions is also computed, using the NUBEAM code [25]. The Maxwellian distributions of the bulk D and T is directly determined from the ion temperature and the D and T density profiles. Hence, a TRANSP simulation contains all the fuel ion distributions required to calculate the neutron spectral components and proceed with the neutron spectroscopy analysis. Note that the plasma rotation is deliberately not included as an input in our TRANSP simulations, it is instead used as a fitting parameter, as detailed in section 3.1.1.

[5] Note that the separation of the neutron spectrum into components is a simplification. This modelling approach is common practice, but it is not an unambiguous description of the spectrum. This is further discussed in section 5.

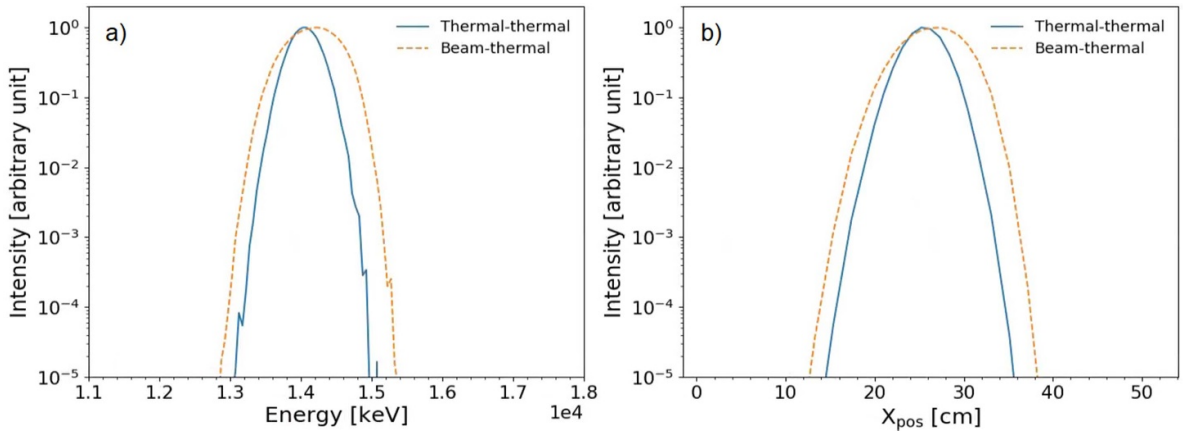


**Figure 4.** Normalized neutron energy spectra for the thermal–thermal and beam–thermal components as calculated by DRESS using the ion distributions from TRANSP, shown as a function of energy in (a) and as a function of hodoscope position in (b) after the detector response function is applied to the spectra. The sharp peaks in the low intensity areas of (a) are due to statistical noise from the Monte Carlo sampling in DRESS. These spectra are calculated for the JET discharge 104 522 in the time interval 7.5–8.0 s.

*3.1.1. Simplifications.* In order to model the neutron spectrum, we are primarily interested in the slowing-down distribution of the NBI ions. Since this work is an exploratory analysis of several discharges, rather than an in-depth analysis of a few discharges, we have used the following modelling simplifications.

(1) The shape of the thermal–thermal spectral component is predominantly determined by the ion temperature [26]. The ion temperature is approximately equal to the electron temperature, and in this analysis, we therefore set $T(i) = T(e)$, where $T(e)$ is obtained from the high-resolution Thomson scattering system at JET [27].
(2) The D and T densities mainly affect the overall intensity of the two spectral components; the effect on their spectral shapes is a higher order contribution that will not be considered in this work. The precise value of the D/T fraction used as input to TRANSP is therefore of little concern in the present analysis; here we have used the D/T ratio inferred from the Penning trap measurements [16].
(3) The influence of RF heating on the modelled distributions can be included in TRANSP by means of a quasi-linear RF kick operator [28]. This makes the process of setting up the simulation more cumbersome and also makes the simulation significantly more computationally expensive. Therefore, it was decided to disregard the effects of RF on the spectral shapes in the present work.

Simplification 1 and 2 do not affect the slowing-down distribution to a first order of approximation, and the impact of simplification 3 is discussed in section 5.1. Ideally, one would want to use the ion temperature instead of relying on simplification 1. However, the ion temperature is typically estimated from CX measurements, which were not available for all the studied discharges. Simplification 1 is therefore used to present comparable results between our selected discharges.

*3.1.2. DRESS.* The DRESS code calculates neutron energy spectra for the thermal–thermal and beam–thermal reactions as separate components, in this instance for neutrons incident on the foil of the MPRu. Examples of calculated neutron energy spectra for the thermal–thermal and beam–thermal components are shown in figure 4(a). DRESS uses Monte Carlo sampling which comes with some statistical noise, this can be seen in the lower intensity areas of figure 4(a). A detector response function is calculated using the same procedure as in [8] for the relevant instrument settings, such as magnetic field strength, foil thickness, and the size of the proton collimator. The detector response function converts the incident neutron spectrum to simulated neutron counts in each hodoscope channel. The normalized simulated spectra on the hodoscope are shown in figure 4(b). Because the intensities of the two spectra are used as fit parameters, see section 3.2, their shapes are the primary result from the calculations using TRANSP, DRESS, and the response function.

*3.1.3. Parameterization.* No bulk plasma rotation information is provided to the TRANSP simulations. Instead, we parameterize the effect of rotation on the neutron spectrum, using the results from [29], which states that a given plasma rotation speed $v_{\mathrm{rot}}$ gives rise to a Doppler shift of the thermal–thermal DT component equal to

$$dE_{\mathrm{rot}} = 0.54 v_{\mathrm{rot}} \cos\alpha \tag{1}$$

where $\alpha$ is the angle between the direction of rotation and the detector LOS ($\alpha \approx 47^\circ$ for the MPRu). This is the energy shift obtained for the thermal–thermal component, i.e. when both reactants come from the rotating bulk plasma. For beam–thermal reactions, only the thermal ions belong to the rotating population and the energy shift for the beam–thermal spectrum component is therefore approximated as $dE_{\mathrm{rot}}/2$.

All in all, the modelling described above constitutes a parameterized model of the neutron spectrum measured by the

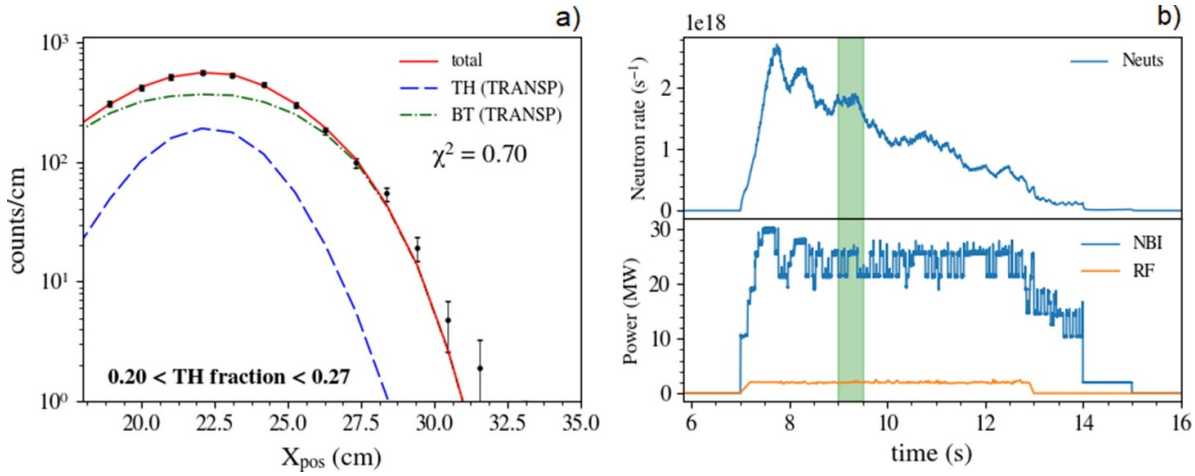


**Figure 5.** In (a) is a completed fit of energy shift and intensity for the thermal–thermal (TH) and beam–thermal (BT) components to the measured hodoscope histogram, shown with black circle markers, for JET plasma discharge 104 689 in the time interval 9.0–9.5 s. Also denoted are the upper and lower bounds for the thermal fraction, given by the statistical uncertainty of the $\chi^2$ fit. In (b) is an overview of the neutron rate (from the JET fission chambers), top panel, and the auxiliary heating power, bottom panel, with the time interval highlighted in green.

MPRu, parameterized in terms of the thermal–thermal and beam–thermal emission intensities, and the energy shift due to plasma rotation.

### *3.2. Fit of model to MPRu data*

The simulated thermal–thermal and beam–thermal hodoscope spectra are fit to match the measured hodoscope histogram from section 2.3. The fit adjusts the intensity of the thermal–thermal and beam–thermal components, as well as the rotation speed. In each iteration a goodness of fit is calculated using $\chi^2$ and the procedure is terminated when the minimal $\chi^2$ is found. Note that the fit interval starts at hodoscope channel 10, excluding the low-energy component, as described in section 2.3. An example of a completed fit is seen in figure 5.

After a completed fit we can extract the thermal fraction $r_{\mathrm{TH}}$ as the ratio

$$r_{\mathrm{TH}} = \frac{I_{\mathrm{TH}}}{I_{\mathrm{TH}} + I_{\mathrm{BT}}} \tag{2}$$

where $I_{\mathrm{TH}}$ and $I_{\mathrm{BT}}$ are the fitted intensities of the thermal–thermal and beam–thermal components, respectively. The rotation speed is obtained from the fitted energy shift, as described in section 3.1. Because the MPRu LOS view is dominated by the plasma core, we approximate the calculated plasma rotation as the on-axis rotation by dividing with the major radius in the core $m$. This expresses the plasma rotation as an angular frequency

$$\omega = \frac{v_{\mathrm{rot}}}{R_0} \tag{3}$$

where $\omega$ is the angular frequency in units of [rad $\mathrm{s}^{-1}$] and $R_0$ is in units of [m].

## 4. Results

The plasma rotation and thermal fraction is estimated for several time intervals in the 10 highest peak neutron rate DTE3 discharges after 104 540, with 104 522 as an addition. The period after 104 540 was chosen to allow for a better comparison between the discharges, since the MPRu magnetic field was fixed at the same value for that entire period. Discharge 104 522 was an extra addition because we had access to a detailed TRANSP simulation which allowed for further analysis, see section 5.1. The detailed simulation included the ion temperature measured by CX spectroscopy, and the effect of RF heating through the RF kick operator. Listed in table 2 are the resulting values for each discharge in the 0.5 s time interval closest to their respective neutron rate peaks (according to the JET fission chambers [30]). The listed uncertainties for the thermal fraction and the plasma rotation are statistical uncertainties from the $\chi^2$ fit, as described in section 3.

For a subset of these discharges, we compare our estimate of the plasma rotation with two CX spectroscopy [10] measurements. One based on neon impurities and the other based on main ions (deuterium) in the plasma. These comparisons are shown in figure 6. Since the neutron emission is typically highest in the plasma core, and since the MPRu LOS passes through the plasma core twice, the MPRu estimates of the rotation and the thermal fraction will be representative of the core values of these parameters. To indicate that the MPRu LOS views more than just the exact plasma centre, it is marked in figure 6 as covering the region from normalized minor radius (rho) equal to 0 up to an arbitrarily selected 0.1.

In figure 7 we showcase time traces for the thermal fraction and the plasma rotation for a selection of JET plasma discharges. Time traces for the other analysed discharges are found in appendix B. The plasma rotation varies between 100 000 and 260 000 rad $\mathrm{s}^{-1}$, and at both the start and end of the discharge the uncertainty is considerably larger

**Table 2.** MPRu estimations of the plasma rotation and thermal fraction around the peak neutron rate.

| JET Plasma discharge # | Time interval [s] | Plasma rotation $\omega$ (rad s$^{-1}$) | Thermal fraction $r_{\mathrm{TH}}$ |
|---|---|---|---|
| 104 522 | 9.0–9.5 | $1.37E5^{+6.2\%}_{-3.4\%}$ | $0.137^{+18\%}_{-18\%}$ |
| 104 551 | 7.5–8.0 | $2.14E5^{+3.5\%}_{-4.0\%}$ | $0.251^{+14\%}_{-14\%}$ |
| 104 574 | 7.5–8.0 | $1.91E5^{+3.5\%}_{-6.8\%}$ | $0.231^{+15\%}_{-15\%}$ |
| 104 575 | 9.0–9.5 | $1.87E5^{+4.6\%}_{-4.2\%}$ | $0.239^{+14\%}_{-14\%}$ |
| 104 664 | 8.0–8.5 | $2.59E5^{+4.5\%}_{-2.7\%}$ | $0.203^{+16\%}_{-16\%}$ |
| 104 674 | 7.5–8.0 | $1.26E5^{+7.2\%}_{-12\%}$ | $0.141^{+15\%}_{-15\%}$ |
| 104 675 | 8.5–9.0 | $1.74E5^{+5.8\%}_{-6.1\%}$ | $0.088^{+31\%}_{-32\%}$ |
| 104 676 | 8.0–8.5 | $2.58E5^{+1.9\%}_{-3.6\%}$ | $0.275^{+9.1\%}_{-9.1\%}$ |
| 104 681 | 7.5–8.0 | $2.49E5^{+3.4\%}_{-4.7\%}$ | $0.047^{+72\%}_{-72\%}$ |
| 104 689 | 7.5−8.0 | $1.86E5^{+5.2\%}_{-8.6\%}$ | $0.112^{+29\%}_{-28\%}$ |
| 104 690 | 8.0–8.5 | $1.91E5^{+2.6\%}_{-4.6\%}$ | $0.294^{+11\%}_{-11\%}$ |

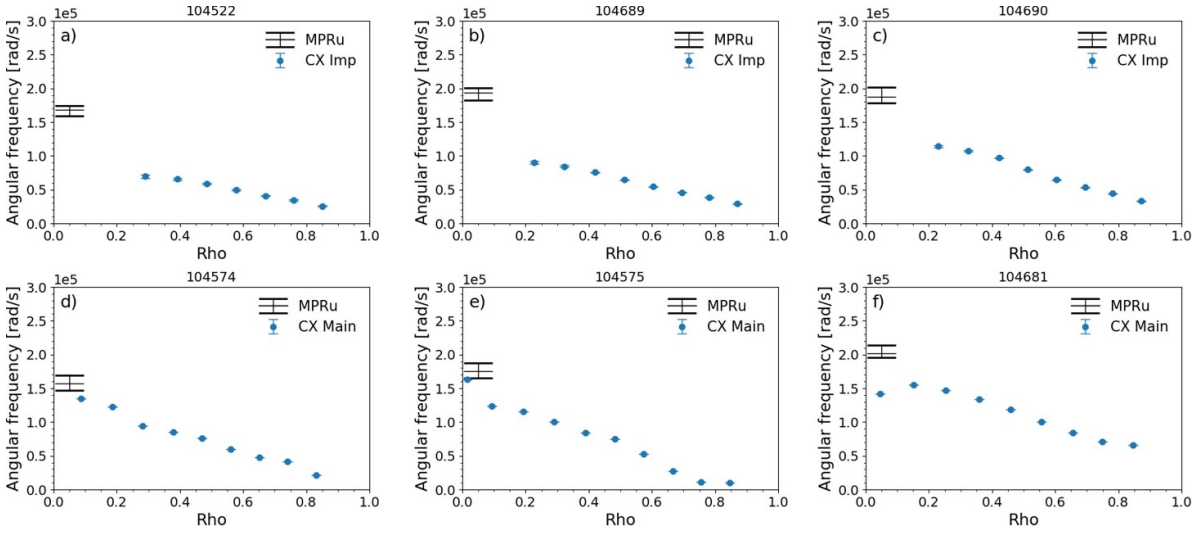


**Figure 6.** Plasma rotation estimated by the MPRu and the CX spectroscopy for a set of plasma discharges in the time interval 9.5–10.0 s. The discharges 104 522 (a), 104 689 (b), and 104 690 (c) use neon impurity CX spectroscopy data. The discharges 104 574 (d), 104 575 (e), and 104 681 (f) use main ion deuterium CX spectroscopy data. Rho denotes the normalized minor radius up to the last closed flux surface.

due to the low number of counts in the MPRu data during these time intervals. The thermal fraction is seen to be around 0.1–0.2 for most of the analysed time intervals, and it never exceeds 0.3.

For some of the analysed data sets, such as the 104 675 data shown in figure 8(a), the measured hodoscope histogram shows a high energy 'tail' for $X_{\mathrm{pos}} \gtrsim 28$ cm. This tail is attributed to the presence of RF-accelerated deuterons in the plasma, which is a well-known phenomenon, seen in many previous experiments [4, 31]. The RF tail is seen to disappear in the subsequent time interval shown in figure 8(c). The time trace of the applied RF heating power is shown or the same time intervals in figures 8(b) and (d), and the RF heating power is indeed off in the latter interval. The RF tail is not present in the modelled spectral components in figure 8, since the RF kick operator was not switched on in TRANSP (cf section 3.1).

## 5. Discussion

In this exploratory analysis, our estimates of the plasma rotation with the MPRu show a higher angular frequency in the core than what a linear extrapolation from the CX data would project, see figure 6. Our estimate had a better agreement with the main ion deuterium CX data compared to the neon impurity CX data. Though as seen in figure 7, the MPRu estimate is consistently higher than the CX data, but the reason for this is not yet fully understood. However, one should note that the comparison was only done for a limited number of plasma discharges. We have yet to make a larger systematic study between the two instruments.

This method has the potential to provide a complementary data point to the CX measurements. The models used in this method can be further refined and currently have several

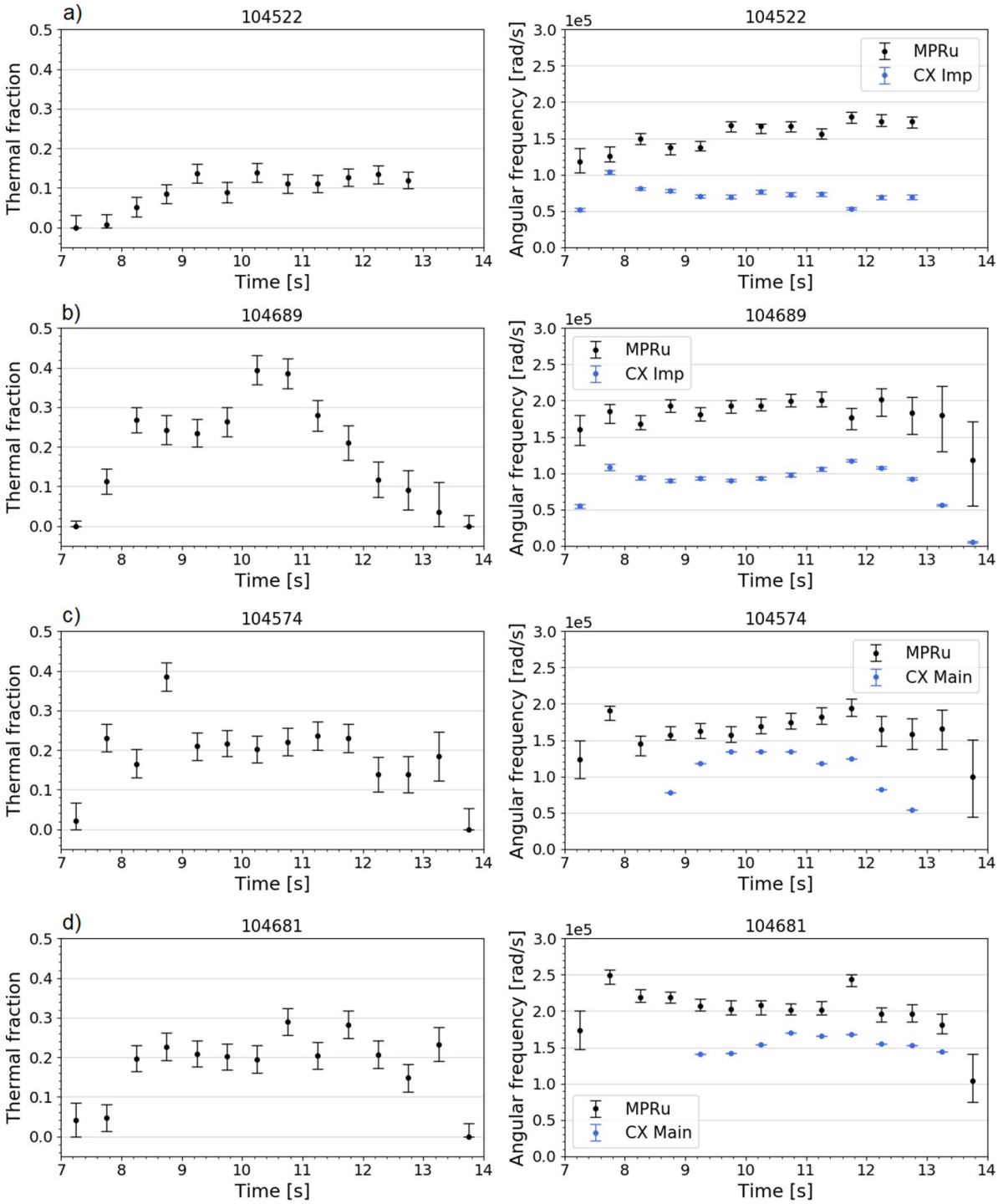


**Figure 7.** Time traces for the thermal fraction (a)–(c) and the plasma rotation (d)–(f) for the JET plasma discharges 104 522, 104 689, and 104 690. The charge exchange data points in (d)–(f) are the estimates closest to the core, see figure 6.

simplifications, see section 3.1.1. With the exception of simplification 3 (discussed below), these simplifications are not expected to have a major impact on the estimates. The most important output from the TRANSP simulation is the shape of the slowing-down distribution of the NBI ions. This distribution is primarily affected by the ion temperature used in the simulation and the heating schemes used. Properties such as the fuel mix or the impurity content, which might be of great importance in other usages of TRANSP simulations, have little to no impact on this method. Another underlying assumption is that the fuel ion velocity distributions can be subdivided into thermal and supra-thermal distributions, thus

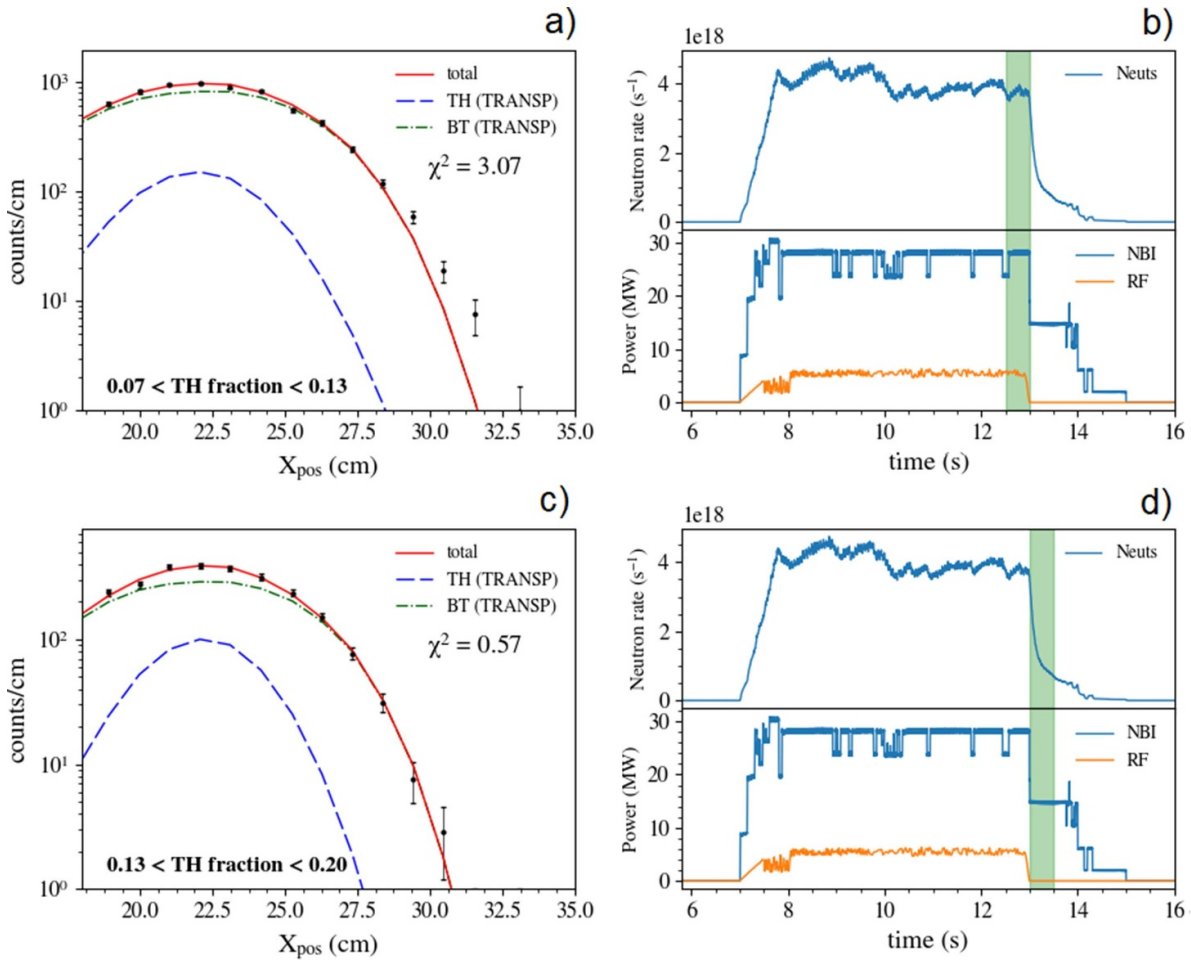


**Figure 8.** Completed fits for JET plasma discharge 104 675 in (a) and (c) for the time intervals 12.5–13.0 s and 13.0–13.5 s respectively. In (b) and (d) are overviews of the neutron rate (from the JET fission chambers) and the auxiliary heating power, with their respective time intervals highlighted in green.

enabling the separation of the neutron spectrum into thermal and beam–thermal spectral components. While this separation is common practice for neutron modelling and data analysis, and by definition necessary for determining the thermal fraction, it does introduce some potential sources of systematic uncertainties in our analysis. Most importantly, the decomposition of the ion distribution into thermal and supra-thermal is not uniquely defined. In this work, we estimate the supra-thermal D distribution with TRANSP/NUBEAM and the thermal D and T distributions as Maxwellians with a prescribed temperature (taken to be the electron temperature). The assumption is then that some superposition of these distributions can give a good description of the actual D and T distributions in the plasma, but this is not guaranteed to be correct. This assumption should be kept in mind, e.g. when comparing the plasma rotation results with other diagnostics that may rely on different assumptions. Analysis methods that do not rely on explicit component separation have also been proposed, see e.g. [32] for further discussion about this.

In future works, this method could be validated by applying it to data where the plasma is not subjected to auxiliary heating (NBI or RF), where a very low plasma rotation is expected. The analysis could also be expanded to include comparisons with JET diagnostics such as x-ray crystal spectroscopy [33] and the single crystal diamond detector that shares LOS with the MPRu [34].

### *5.1. The effect of RF heating*

In some instances, the MPRu estimate is likely to overestimate the plasma rotation. This is seen in figure 8 where the model does not describe the high energy RF tail, which can therefore be expected to skew the estimate towards a higher energy shift, and subsequently a higher fitted plasma rotation. This is due to simplification 3 in section 3.1.1, which could be addressed by using a more extensive TRANSP simulation that includes the RF heating. We have performed an

initial comparison between our simplified TRANSP simulation and one that both includes the RF kick operator and measurements of the ion temperature from CX measurements. For plasma discharge 104 522, the angular frequency using the simplified TRANSP simulation was on average 21% higher than for the more extensive TRANSP simulation. Using the RF kick operator brought the MPRu estimate closer to the CX estimate of the plasma rotation. For the discharges in figures 7(c) and (d), a downshift of around 21% could bring the MPRu estimate in line with the main ion deuterium CX data.

### 5.2. Thermal fraction

The thermal fraction estimates had an average relative uncertainty of 22% and a median uncertainty of 15%. The large relative uncertainty of plasma discharge 104 681 is an outlier in table 2 due to the relatively low value of the thermal fraction in that time interval. Additional time intervals for 104 681 are shown in (a) (appendix B), where it is clear that the absolute uncertainties are not significantly larger than those in figures 7(a)–(c), or in figures 11–17.

According to the thermal fraction estimates, the beam–thermal component clearly dominated over the thermal–thermal component for all discharges reviewed in this paper. In contrast, the same kind of estimates with the MPR during the JET DTE1 campaign observed several discharges where the thermal–thermal component dominated instead [35]. This was likely due to higher ion temperatures for those discharges (15–20 keV, compared to 10–12 keV in the DTE3 discharges studied here).

Furthermore, the NBI energy was often as high as 150 keV for discharges during the DTE1 campaign, compared to the current level around 80–100 keV. The higher beam energies broadened the beam–thermal component, which simplified the separation between it and the thermal–thermal component, compare figure 1 in [36] to figure 5 in the present paper. While the MPRu system is still able to estimate the thermal fraction under the current circumstances, this complicating connection to the beam energy should be kept in mind for future neutron spectroscopy designs.

### 5.3. Data reduction

In the data reduction routine, the event selection can be improved by incorporating the escape events. This can be done by developing correction factors for the omitted escape events based on the simulations in [15]. According to that study, the correction factors will differ between the four phoswich scintillator types used in the hodoscope [8], which means that the inclusion of escape events will somewhat alter the shape of the hodoscope histogram. Alternatively, characterizing the background events could allow us to estimate the number of escape events where they overlap with the background in the PSD histogram. A background characterization would also improve event counting in the higher channels, where the events in the proton peak are too few to distinguish from the background. The data reduction could be further improved by characterizing the low energy component, which would allow the use of all active hodoscope channels.

## 6. Conclusions

We have created the framework for a method that uses MPRu data to estimate the plasma rotation and the thermal fraction in plasma discharges from the recent JET DTE3 experimental campaign. These two quantities are estimated in the core, which has the potential to complement measurements from other diagnostics, such as CX spectroscopy. The thermal fraction and the plasma rotation can aid in the analysis of plasma discharges, either directly or by validating interpretative plasma modelling codes such as TRANSP. The method could also guide the execution of future fusion experiments, and potentially provide estimates to operators in real time. The estimates presented in this paper can be further improved by incorporating more refined modelling of the neutron spectral shapes (e.g. using the RF kick operator in TRANSP) in the analysis.

## Data availability statement

The data cannot be made publicly available upon publication because they are owned by a third party and the terms of use prevent public distribution. The data that support the findings of this study are available upon reasonable request from the authors.

## Acknowledgment

This work has been carried out within the framework of the EUROfusion Consortium, funded by the European Union via the Euratom Research and Training Programme (Grant Agreement No. 101052200—EUROfusion). Views and opinions expressed are however those of the author(s) only and do not necessarily reflect those of the European Union or the European Commission. Neither the European Union nor the European Commission can be held responsible for them.

This work was assisted by Sheena Menmuir regarding accessing and analysing charge exchange data.

## Appendix. A

Additional 2D PSD histograms are shown in figures 9 and 10 for hodoscope channels 17 and 20 respectively.

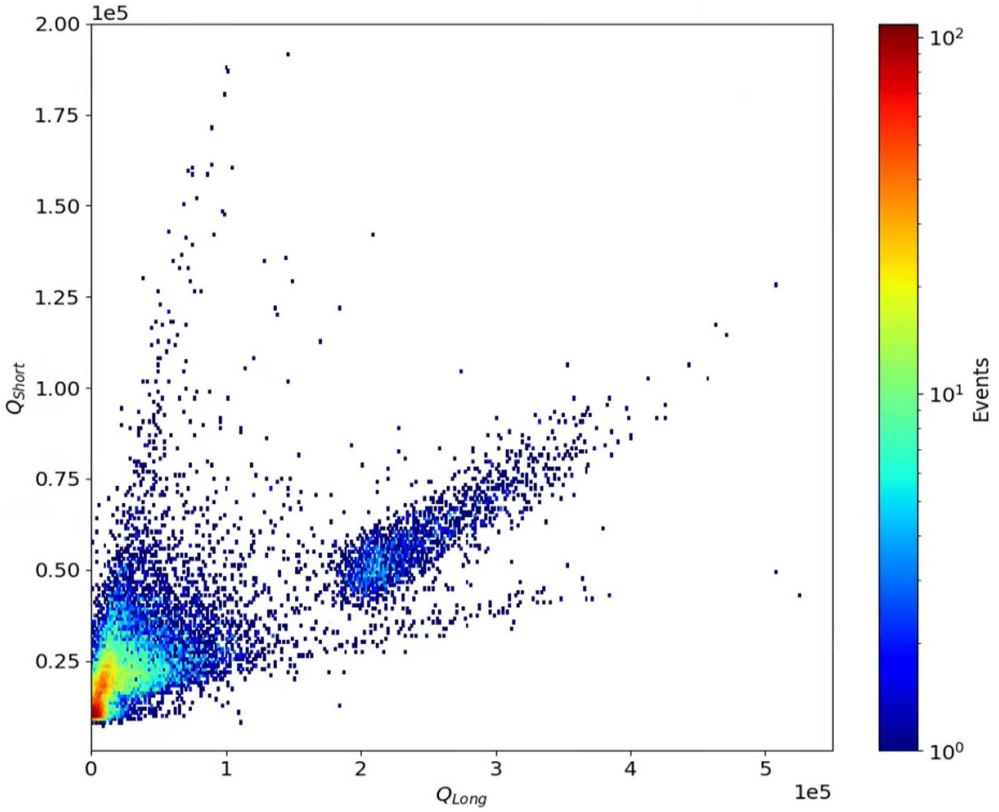


**Figure 9.** 2D PSD histogram for JET plasma discharge 104 681, channel 18, in the time interval 7.0–15.0 s. The proton peak is elongated and much closer to the background than for other channels. This is likely due to a high voltage failure for one of the two photomultiplier tubes for this channel, alternatively there could be a problem with the light guide's optical connection.

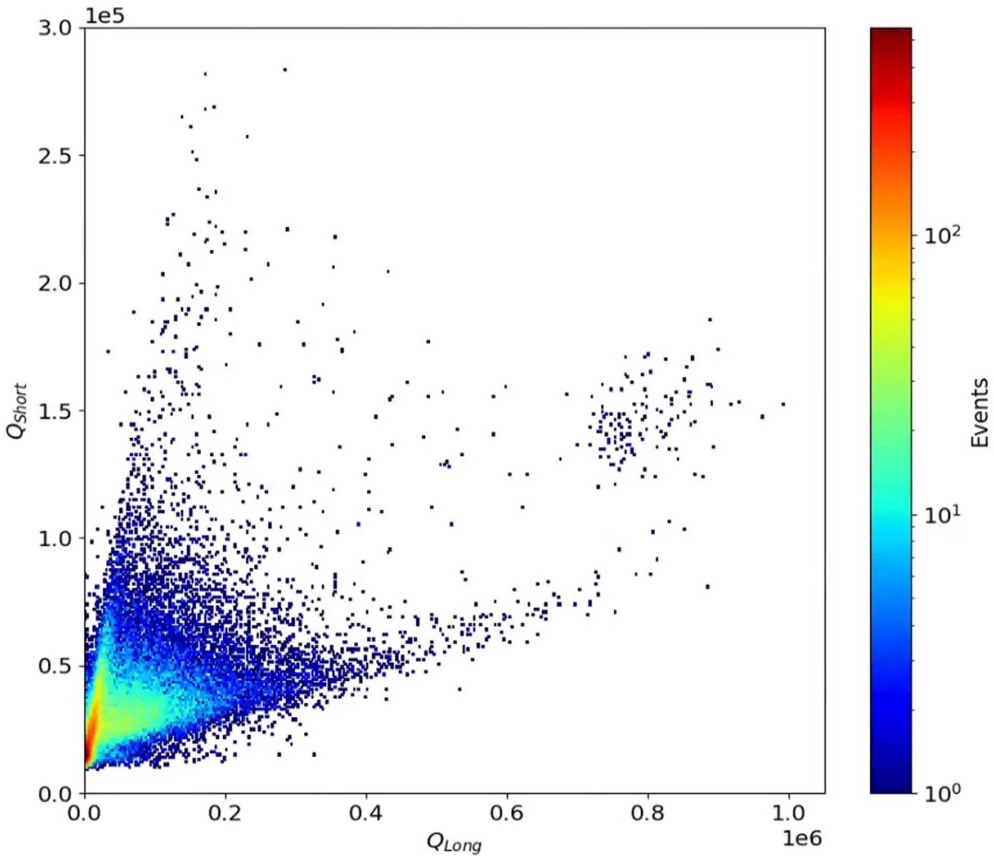


**Figure 10.** 2D PSD histogram for JET plasma discharge 104 681, channel 21, in the time interval 7.0–15.0 s. Due to the low count rate, the proton peak becomes increasingly difficult to distinguish from the background.

## Appendix. B

Time traces for the thermal fraction and plasma rotation estimates for shots 104 551, 104 574, 104 664, 104 674, 104 575, 104 664, 104 674, 104 676, 104 681 and 104 690 are found in figures 11–17.

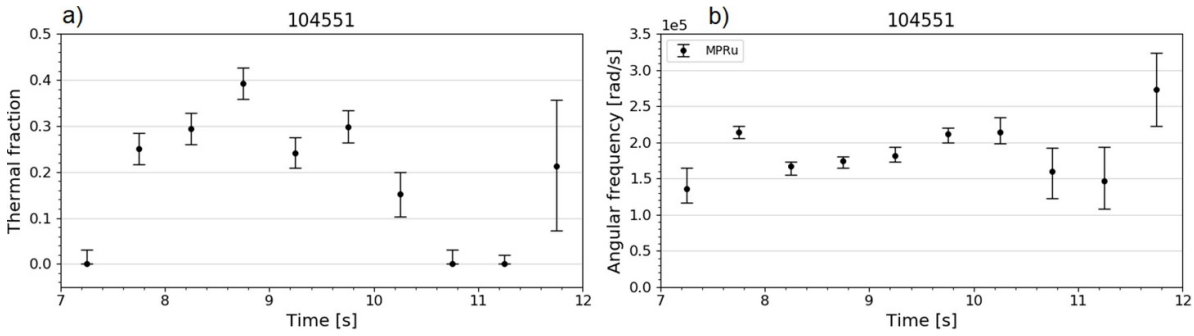


**Figure 11.** Time traces for the thermal fraction (a) and the plasma rotation (b) for the JET plasma discharge 104 551.

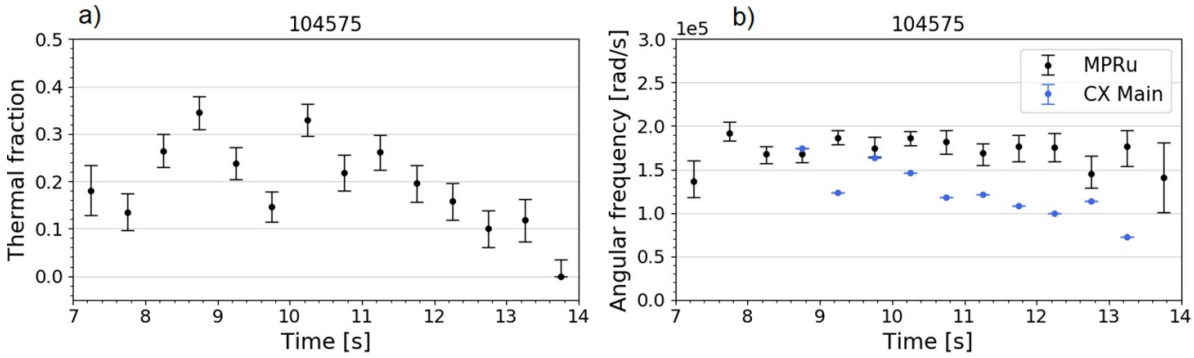


**Figure 12.** Time traces for the thermal fraction (a) and the plasma rotation (b) for the JET plasma discharge 104 575.

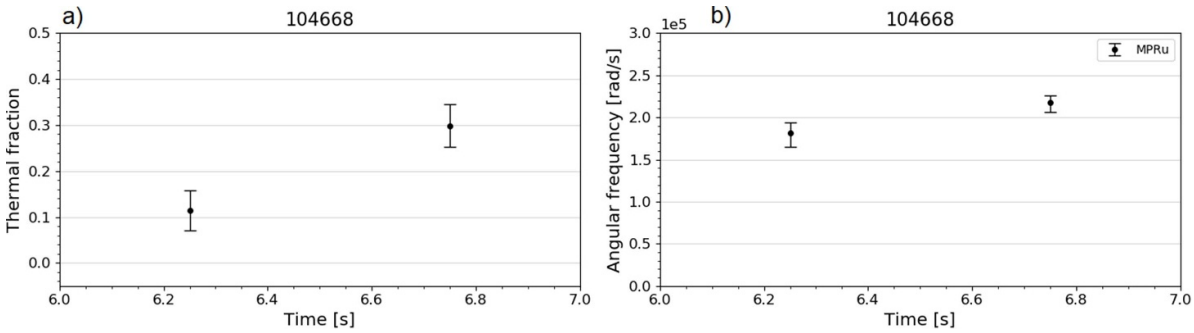


**Figure 13.** Time traces for the thermal fraction (a) and the plasma rotation (b) for the JET plasma discharge 104 668.

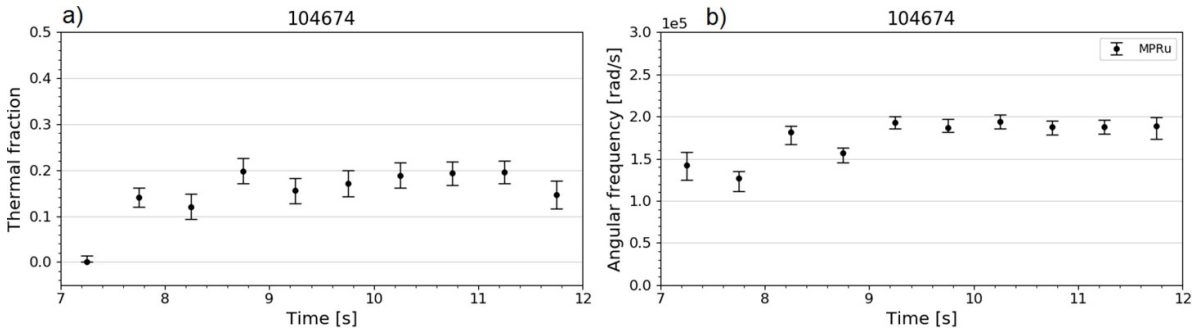


**Figure 14.** Time traces for the thermal fraction (a) and the plasma rotation (b) for the JET plasma discharge 104 674.

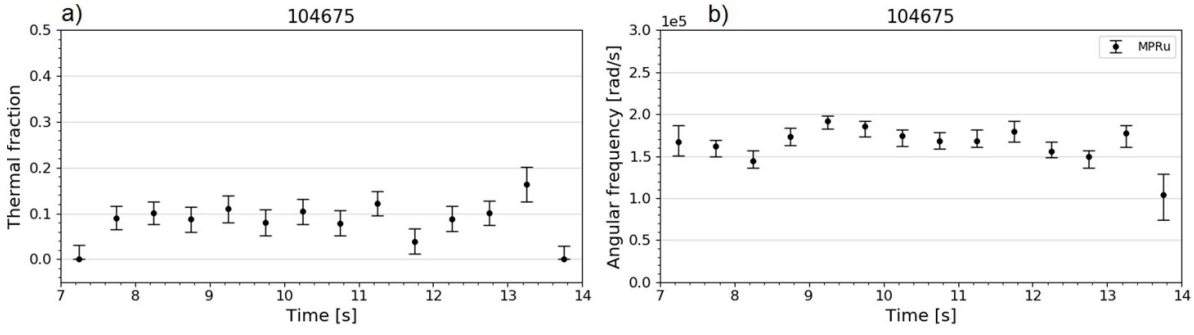


**Figure 15.** Time traces for the thermal fraction (a) and the plasma rotation (b) for the JET plasma discharge 104 675.

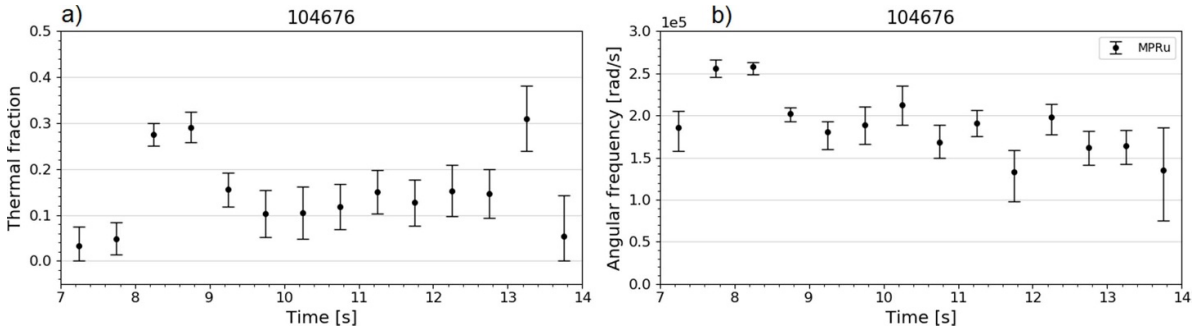


**Figure 16.** Time traces for the thermal fraction (a) and the plasma rotation (b) for the JET plasma discharge 104 676.

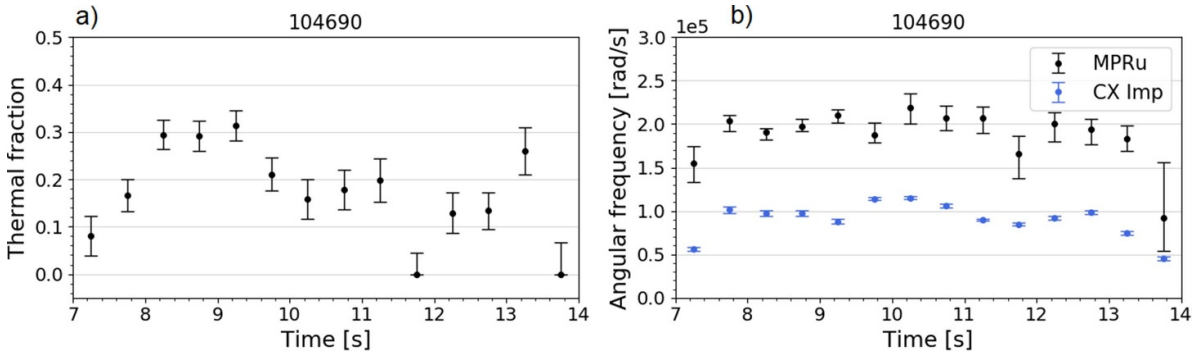


**Figure 17.** Time traces for the thermal fraction (a) and the plasma rotation (b) for the JET plasma discharge 104 690.

## ORCID iDs

Linus Hägg https://orcid.org/0000-0002-0789-505X
Jacob Eriksson https://orcid.org/0000-0002-0892-3358
Erik Andersson Sundén https://orcid.org/0000-0002-8501-8642

## References

[1] Källne J, Ballabio L, Frenje J, Conroy S, Ericsson G, Tardocchi M and Traneus E 2000 Observation of the alpha particle 'knock-on' neutron emission from magnetically confined DT fusion plasmas *Phys. Rev. Lett.* **85** 1246
[2] Eriksson J *et al* Calculation of α knock-on neutron spectra from JET DT plasmas *49th EPS Conf. on Contr. Fusion and Plasma Phys.* (*3–7 July 2023*)
[3] Henriksson H, Conroy S, Ericsson G, Giacomelli L, Gorini G, Hjalmarsson A, Källne J, Tardocchi M and Weiszflog M 2005 Systematic spectral features in the neutron emission from NB heated JET DT plasmas *Plasma Phys. Control. Fusion* **47** 1763
[4] Henriksson H, Conroy S, Ericsson G, Gorini G, Hjalmarsson A, Källne J, Tardocchi M and Weiszflog M 2006 Synergetic RF and NB heating effects in JET DT plasmas studied with neutron emission spectroscopy *Nucl. Fusion* **46** 244
[5] Frenje J, Ballabio L, Conroy S, Ericsson G, Gorini G, Källne J, Prandoni P, Tardocchi M and Traneus E 1999 Neutron emission Doppler-shift measurements in deuterium–tritium plasmas *Rev. Sci. Instrum.* **70** 1176–80
[6] Järleblad H *et al* 2025 Reconstruction of the fast-ion deuterium distribution in a tritium-rich plasma in the JET DTE2 campaign *Nucl. Fusion* **65** 01606
[7] Salewski M *et al* 2017 MeV-range velocity-space tomography from gamma-ray and neutron emission spectrometry measurements at JET *Nucl. Fusion* **57** 056001
[8] Andersson Sundén E *et al* 2009 The thin-foil magnetic proton recoil neutron spectrometer MPRu at JET *Nucl. Instrum. Methods Phys. Res.* A **610** 682–99
[9] Eurofusion Breaking new ground: JET Tokamak's latest fusion energy record shows mastery of fusion processes (available at: https://euro-fusion.org/eurofusion-news/dte3record/) (Accessed 12 April 2024)
[10] von Hellermann M G, Mandi W, Summers H P, Weisen H, Bolieau A, Morgan P D, Morsi H, Koenig R, Stamp M F and Wolf R 1990 Visible charge exchange spectroscopy at JET *Rev. Sci. Instrum.* **61** 3479–86
[11] de Vries P C *et al* 2006 Plasma rotation and momentum transport studies at JET *Plasma Phys. Control. Fusion* **48** 1693
[12] Knoll G F 1999 *Radiation Detection and Measurements* (Wiley)
[13] Ronchi E, Conroy S, Andersson Sundén E, Ericsson G, Gatu Johnson M, Hellesen C, Källne J, Sjöstrand H and Weiszflog M Development and implementation of pulse summing amplifier modules for the MPRu fusion neutron spectrometer at JET the DiVa portal (available at: https://urn.kb.se/resolve?urn=urn:nbn:se:uu:diva-109477) (Accessed 22 August 2024)
[14] Teledyne SP Devices ADQ14—multi-channel, 14-bit digitizer (available at: www.spdevices.com/what-we-do/products/hardware/14-bit-digitizers/adq14) (Accessed 20 August 2024)
[15] Wikström G 2005 Performance studies of phoswich detectors in the upgraded magnetic proton recoil neutron spectrometer
[16] Hillis D L, Klepper C C, Von Hellermann M, Ehrenberg J, Finken K H and Mank G 1997 Deuterium-tritium

concentration measurements in the divertor of a tokamak via a modified Penning gauge *Fusion Eng. Des.* **34–35** 347–51
[17] Hobirk J *et al* 2023 The JET hybrid scenario in deuterium, tritium, and deuterium-tritium *Nucl. Fusion* **63** 112001
[18] Maslov M *et al* 2023 JET D-T scenario with optimized non-thermal fusion *Nucl. Fusion* **63** 112002
[19] Mantsinen M J *et al* 2023 Experiments in high-performance JET plasmas in preparation of second harmonic ICRF heating of tritium in ITER *Nucl. Fusion* **63** 112015
[20] Fitzgerald M *et al* 2022 Toroidal Alfvén eigenmode stability in JET internal transport barrier afterglow experiments *Nucl. Fusion* **62** 106001
[21] Eriksson J, Conroy S, Andersson Sundén E and Hellesen C 2016 Calculating fusion neutron energy spectra from arbitrary reactant distributions *Comput. Phys. Commun.* **199** 40–46
[22] Pankin A Y, Breslau J, Gorelenkova M, Andre R, Grierson B, Sachdev J, Goliyad M and Perumpilly G 2024 TRANSP integrated modeling code for interpretive and predictive analysis of tokamak plasmas (arXiv:2406.07781 [physics.plasm-ph])
[23] TRANSP website TRANSP PPPL (available at: https://transp.pppl.gov/) (Accessed 6 September 2024)
[24] Hellesen C *et al* 2008 Validating TRANSP simulations using neutron emission spectroscopy with dual sight lines *Rev. Sci. Instrum.* **79** 10E510
[25] Pankin A, McCune D, Andre R, Bateman G and Kritz A 2004 The tokamak Monte Carlo fast ion module NUBEAM in the National Transport Code Collaboration library *Comput. Phys. Commun.* **159** 157–84
[26] Brysk H 1973 Fusion neutron energies and spectra *Plasma Phys.* **15** 611–7
[27] Pasqualotto R, NiIelsen P, Gowers C, Beurkens M, Kempenaars M, Carlstrom T and Johnson D 2004 High resolution Thomson scattering for Joint European Torus (JET) *Rev. Sci. Instrum.* **75** 3891–3
[28] Kwon J, McCune D and Chang C S Enhancement of NUBEAM for the simulation of fast ion and RF-wave interaction based on the quasi-linear theory (available at: http://meetings.aps.org/link/BAPS.2007.DPP.UP8.83) (Accessed 6 September 2024)
[29] Gorini G, Källne J and Ballabio L 1997 Neutron spectrometry for plasma rotation *Rev. Sci. Instrum.* **68** 561–4
[30] Syme D B, Popovichev S, Conroy S, Lengar I and Snoj L JET EFDA Contributors 2012 Fusion yield measurements on JET and their calibration *Nucl. Eng. Des.* **246** 185–90
[31] Hellesen C, Mantsinen M, Conroy S, Ericsson G, Eriksson J, Kiptily V G and Nabais F 2018 Analysis of resonant fast ion distributions during combined ICRF and NBI heating with transients using neutron emission spectroscopy *Nucl. Fusion* **58** 056021
[32] Salewski M *et al* 2018 Deuterium temperature, drift velocity, and density measurements in non-Maxwellian plasmas at ASDEX Upgrade *Nucl. Fusion* **58** 036017
[33] Nave M F F *et al* Measuring instrinsic rotation in the JET tokamak *42nd EPS Conf. on Plasma Physics* (*22–26 June 2015*)
[34] Rigamonti D *et al* 2024 The single crystal diamond-based diagnostic suite of the JET tokamak for 14 MeV neutron counting and spectroscopy measurements in DT plasmas *Nucl. Fusion* **64** 016016
[35] Hellesen C, Eriksson J, Binda F, Conroy S, Ericsson G, Hjalmarsson A, Skiba M and Weiszflog M 2015 Fuel ion ratio determination in NBI heated deuterium tritium fusion plasmas at JET using neutron emission spectrometry *Nucl. Fusion* **55** 023005
[36] Hellesen C, Eriksson J, Conroy S, Ericsson G, Skiba M and Weiszflog M 2012 Fuel ion ratio measurements in reactor relevant neutral beam heated fusion plasmas *Rev. Sci. Instrum.* **83** 10D916